scientific reports

Check for updates

OPEN

A novel approach for high impedance fault detection in resonant grounding systems based on statistical characteristics

Qinglin Meng[1,2,3]✉, Yuan Gao[1,4]✉, Sheharyar Hussain[1]✉, Ying He[1]✉ & Botong Li[2]✉

High impedance faults (HIF) in the resonant grounding system of distribution networks pose significant challenges for traditional protection devices, which often fail to detect and eliminate these faults promptly. The difficulty in setting an appropriate threshold and ensuring reliable detection at low signal-to-noise ratios further complicates the issue. To overcome these limitations, this paper presents a novel approach that analyzes the kurtosis and skewness characteristics of the single-phase high-impedance grounding zero-sequence current waveform, using the Emanuel model as a basis. The proposed method detects HIF based on a kurtosis threshold and pinpoints the faulted line using the skewness coefficient, introducing a more reliable and precise detection technique. Simulation and field tests validate the robustness of this approach, demonstrating strong resistance to noise interference and enhanced fault detection capabilities.

Keywords Resonant grounding system, Distribution network, Fault detection, Faulty line selection, High impedance fault

Abbreviations

α	Count index of the sampling window in a power-frequency period
f_s	Sampling frequency of the zero-sequence current (Hz)
I_c	System grounding capacitive current (A)
i_0	Zero-sequence current (A)
i_{0q}	Zero-sequence current of feeder q (A)
$i(N)$	Sampled zero-sequence current sequence at sample index N (A)
j	Cycle index in the observation window
$K_1 - K_4$	Kurtosis coefficients of the zero-sequence current for lines $L_1 - L_4$ in a given condition
$K_{i0}(T_\alpha/2), q$	Half-cycle kurtosis of the zero-sequence current of feeder q in sampling window α
$L_1 - L_4$	Four feeders (lines) in the studied distribution network
$M_{01} - M_{04}$	Mean half-cycle skewness indices of lines $L_1 - L_4$
$M_{0q}(j)$	Half-cycle skewness of zero-sequence current of feeder q in cycle j
m	Total number of lines/feeders in the network
N	Number of samples per power-frequency cycle
N_h	Number of samples per half-cycle
P	Kurtosis variance index used for HIF discrimination
Pset	Threshold value of the kurtosis variance index
p_{oq}	Mean full-cycle skewness of feeder q over the observation window
q	Index of a specific feeder or line
q_{0q}	Mean half-cycle skewness of feeder over the observation window
R_f	Fault transition resistance between conductor and ground (Ω or kΩ)
$S_{01} - S_{04}$	Mean full-cycle skewness indices of lines

[1]Green Power Research Institute, Tianjin Renai College, Tianjin 301636, China. [2]School of Electrical and Information Engineering, Tianjin University, Tianjin 300072, China. [3]State Grid Tianjin Electric Power Company, State Grid Corporation of China, Tianjin 300010, China. [4]School of Electrical Engineering, Zhejiang University, Hangzhou 310007, China. ✉email: qinglin.meng@ieee.org; gaoyuan2000@ieee.org; ee.sbangash@zju.edu.cn; heying@tjrac.edu.cn; libotong@tju.edu.cn

$S_{0q}(j)$	Full-cycle skewness of zero-sequence current of feeder q in cycle j
T	Fundamental power-frequency period (s)
U_0	Zero-sequence voltage of the busbar (V)
U_{ph}	Phase (line-to-neutral) voltage (V)
V_n	Negative DC equivalent voltage source in the Emanuel HIF model (V)
V_p	Positive DC equivalent voltage source in the Emanuel HIF model (V)
x_i	i-th sampled value of a data sequence
$\overline{x}$	Mean value of a data sequence
Z	Starting index of the sampling window in a period
μ	Mean or first central moment of a data sequence
μ_r	r-th central moment of a data sequence
σ	Standard deviation of a data sequence
σ^2	Variance of a data sequence

Electricity distribution networks often operate in complex environments with various potential hazards. Single-phase high-impedance grounding faults frequently occur due to non-ideal conductors such as tree branches, sand, or water bodies like ponds [1]. If these faults are not promptly addressed, they may escalate into phase-to-phase or short-circuit faults, endangering the safety of the power system and posing risks to human lives [2–4]. Hence, the timely identification and management of high-impedance grounding faults are crucial. In parallel, advanced condition monitoring strategies in gear transmission systems and power electronic devices have shown that combining innovative sensing structures with data-driven indicators can significantly enhance early fault awareness and operational reliability [5,6]. However, detecting these faults proves more challenging compared to low-impedance faults (LIFs), due to factors such as large transition impedance, weak fault currents, and unstable fault locations. This challenge is particularly pronounced in resonant grounding systems [7].

Recent years have seen significant advancements in the study of high-impedance grounding fault detection. Most research can be categorized into three main methodologies: time-domain analysis, frequency-domain analysis, and time-frequency domain analysis. Based on the non-linear impedance of high-impedance grounding faults, a study [8] analyzed the volt-ampere characteristic curve at fault points and utilized its slope as a detection criterion. Another study employed the concave-convex pattern resulting from the arc thermal effect of zero-sequence current near zero-crossing points to detect these faults, though its robustness diminishes under interference. In [9], zero-sequence current was projected onto zero-sequence voltage, while studies [10–12] extracted characteristic quantities from irregular signal waveforms using mathematical morphology. These approaches predominantly analyzed high impedance faults (HIF) zero-sequence current waveforms exhibiting random properties. However, in resonant grounding systems, the fault characteristic quantities are small and difficult to measure accurately due to noise interference and instrument limitations, which hinders the extraction of time-domain features. Another study [13] detected faults using the magnitude and phase of the third harmonic, alongside the magnitude of the second and fifth harmonics. Research [14] utilized the discrete Fourier transform to analyze inter-harmonics close to the fundamental frequency, proposing a detection method based on the root-mean-square value of the inter-harmonics. Study [15] examined the zero-sequence equivalent circuit of HIF and proposed a line selection method based on differences in transient components and fault current flow direction.

However, the harmonic content of HIF current varies considerably with the grounding medium, making it challenging to define a precise threshold, especially under low signal-to-noise (SNR) conditions. Detection methods in the time-frequency domain, such as wavelet transform, integrate time and frequency domain information, helping to mitigate interference. Wavelet transform is the most commonly used time-frequency domain method. More recently, chirplet-transform-based and reassigned time–frequency techniques have been employed to extract weak and time-varying fault indicators in complex rotating machinery and gearboxes, further underscoring the importance of high-resolution time–frequency representations for nonstationary fault signatures [16,17]. In [18], wavelet transformation was applied to obtain the energy spectrum of high- and low-frequency components of zero-sequence voltage signals, enabling the detection of HIFs based on a threshold. Study [19] utilized the wavelet transform results of zero-sequence voltage and current to develop a line selection criterion, while [20] introduced a new feature for HIF detection by analyzing zero-sequence current using wavelet transform. Further research [21] differentiated HIFs from other transient signals by comparing the high-frequency energy spectrum of zero-sequence current. Despite its effectiveness in representing local features in both time and frequency domains, wavelet transform-based HIF detection relies on high-frequency components, making it less reliable in environments with a low SNR ratio.

Although significant strides have been made in detecting HIF, existing methods frequently face challenges related to computational efficiency and accuracy, especially in noisy environments. In addition, learning-based fault diagnosis frameworks, including interval type-2 fuzzy neural networks and physically interpretable wavelet-guided networks, have been proposed to model complex nonlinear degradation behaviors, but they typically require extensive labeled data and higher computational resources [22,23]. This paper seeks to overcome these challenges by introducing a novel decision-making approach that improves both the reliability and speed of fault detection. By leveraging kurtosis and skewness coefficients, the proposed method achieves precise fault classification while keeping computational demands low. The following sections provide an in-depth analysis of this approach, validated through simulations and field tests.

Key contributions of this work include:

1) A new approach utilizing kurtosis and skewness coefficients for diagnosing single-phase high-impedance grounding faults, ensuring accurate fault characteristic identification.

2) The introduction of a decision-making method that uses zero-sequence current data to accurately classify faults and identify the faulted line with minimal computational cost.

3) Demonstration of the method's superior performance through simulations and field tests, highlighting its strong anti-noise capability and reduced computational complexity compared to existing algorithms.

The remaining paper is organized as follows: Section 2 provides an analysis of HIF, discussing the resonant grounding system, fault characteristics, and the proposed kurtosis-based method. Section 3 covers the simulation analysis, including model setup, threshold setting, and validation under noise. Section 4 presents field test results, and Section 5 concludes with key findings and future directions.

Decision-making analysis of HIF

Resonant grounding system

In a resonant grounding system, the neutral point is grounded via an arc suppression coil. When a fault occurs, the residual current from the system's capacitive current, post-compensation, becomes minimal [8], effectively suppressing arc overvoltage. As a result, the grounding arc does not meet the conditions for resignation and extinguishes naturally. Additionally, the system can remain operational during a fault, continuing to supply power for up to two hours, which enhances the reliability of the power supply. However, since the arc suppression coil typically operates in an over-compensation mode, the fault current becomes significantly weakened, and the zero-sequence current direction can change abruptly at certain points. This renders traditional line selection methods, which rely on amplitude and polarity, ineffective. Therefore, fault line selection and accurate location in resonant grounding systems remain a focus for power engineers.

HIF characteristics

When a high-impedance ground fault occurs in a distribution network, an arc forms. Due to the non-linearity of the grounding medium, the transition impedance fluctuates as the arc burns, leading to diverse fault current characteristics. The key features of this type of fault are as follows:

1) **Non-linearity:** The volt-ampere characteristic curve of the voltage and current is not linear due to the non-linear nature of the fault impedance.

2) **Asymmetry:** The waveforms of the fault current's positive and negative half cycles differ.

3) **Intermittency:** The fault current is temporarily interrupted at the zero-crossing point due to unstable arc combustion and non-linearity in the grounding medium.

4)**Weak fault current:** The high transition impedance in HIF results in a very low fault current, making it difficult for conventional protection systems to detect and operate.

Accurate detection of HIF requires an appropriate fault model. Given the complex and variable nature of distribution network operations, HIF are influenced by numerous random factors. In recent years, extensive research has been conducted on HIF modeling. The high-impedance model used in this study is based on the work [24], developed through arc fault experiments on sand. The model includes two anti-parallel DC voltage sources, V_p and V_n, to replicate the asymmetry and intermittent nature of the fault current. When the phase voltage exceeds V_p, current flows to the ground. When the phase voltage falls below $-V_p$, current flows in the reverse direction. No current flows when the phase voltage is between these values. Additionally, to simulate non-linear impedance, the model includes two resistors of different sizes in series with the voltage sources, producing fault currents of varying magnitudes.

Analysis of kurtosis coefficient-based decision-making method

The kurtosis coefficient is a statistical measure that characterizes the distribution of random variables. It is highly sensitive to signal variations, allowing it to detect high-frequency spikes in a signal independent of its absolute magnitude. The discrete fourth-order central moment, used to compute the kurtosis coefficient, is expressed by the following formula [25]:

$$K = 1/n\sum_{i=1}^{i=n}((x_i - \bar{x})/\sigma)^4 \tag{1}$$

In (1), n represents the number of data points in the group, x_i is the value of each sampled signal point, $\overline{x}$ is the mean value of the signal, and $\sigma$is the standard deviation of the signal, which is calculated using the formula shown in (2).

$$\sigma = \sqrt{\frac{1}{n}\sum_{i=1}^{i=n}(x_i - \bar{x})}^2 \tag{2}$$

In the case of a low impedance ground fault within a resonant grounding system, the zero-sequence current waveform typically consists of power frequency components and attenuated DC components. The attenuation of the DC component over one cycle is minimal, resulting in a nearly sinusoidal current waveform. The positive and negative half-cycles of this waveform maintain symmetry throughout the cycle. When considering the absolute value of the sampling time, the waveform's cycle equals half of the power frequency cycle. The kurtosis values for

both half-cycle and full-cycle data are generally consistent. As a result, when a LIF continues for multiple cycles, the kurtosis magnitude, calculated at intervals of half the power frequency cycle, remains relatively constant.

In contrast, when a high-impedance grounding fault occurs, the non-linear variation of the transition impedance causes asymmetry in the zero-sequence current waveform. The waveforms of the positive and negative half-cycles differ, leading to varying kurtosis coefficient values when calculated for each half-cycle.

To minimize the impact of abnormal data and random outliers, the zero-sequence current waveform is sampled after all line transient processes have settled, and the kurtosis index is formed by averaging multiple consecutive half-cycle calculations so that the decision is driven by persistent distortion rather than isolated spikes. Let N represent the number of sampling points per power frequency, m be the total number of lines, q denote a specific line among m, α be the count value for the sampling period, and Z represent the total count for the sampling period. Finally, $i\,(N)$refers to the sampled zero-sequence current sequence. The kurtosis calculation is performed as follows:

$$K_{i0(\frac{T\alpha}{2}),q}=\frac{\sum_{N=\frac{T\alpha}{2}}^{N=\frac{T}{2}(1+\alpha)}\left(\frac{|i(N)|-\mu_{\frac{T\alpha}{2},q}}{\sigma_{\frac{T\alpha}{2},q}}\right)^4}{\frac{N}{2}} \tag{3}$$

$$\text{where } \mu_{T\alpha/2,q}=\frac{2}{N}\sum_{N=\frac{T\alpha}{2}}^{N=\frac{T}{2}(1+\alpha)}|i\,(N)|?\text{and } \sigma_{T\alpha/2,q}=\sqrt{\frac{2}{N}\sum_{N=\frac{T\alpha}{2}}^{N=\frac{T}{2}(1+\alpha)}(|i\,(N)|-\mu_{T\alpha/2,q})^2}.$$

.

The preceding analysis indicates that the half-cycle kurtosis of the zero-sequence current fluctuates in high-impedance grounding faults, while it remains relatively constant in LIFs. A noticeable difference in the variance of these fluctuations is expected between the two fault types. As a result, the average value P of the zero-sequence current kurtosis variance can serve as a characteristic value for identifying high-impedance grounding faults. The calculation process is provided in (4) and (5).

$$\sigma_{i0(T\alpha/2),q}=\sqrt{\frac{1}{(\alpha+1)}\left(\sum_{\alpha=0}^{\alpha=Z}(K_{i0(T\alpha/2),q}-\mu_{k,q})^2\right.} \tag{4}$$

$$P=\frac{\sum_{q=1}^{q=m}\sigma_{i0(T\alpha/2),q}}{m} \tag{5}$$

where $\mu_{k,q}=\frac{1}{(a+1)}\sum_{\alpha=0}^{\alpha=Z}K_{i0(T\alpha/2),q}$.

Analysis of skewness coefficient-based decision-making method

The skewness coefficient is a statistical measure used to describe the symmetry of a data set's overall value distribution. If the distribution follows a normal shape, the skewness is 0. When the data distribution is skewed to the right compared to the normal distribution, the skewness is greater than 0. Conversely, if the distribution is left-skewed, the skewness is less than 0. The skewness is calculated using the discrete third-order central moment, as expressed by the following formula:

$$S=\frac{1}{n-1}\sum_{i=1}^{i=n}\frac{(x_i-\overline{x})^3}{\sigma^3} \tag{6}$$

When a high-impedance grounding fault occurs in the distribution network, the zero-sequence current signal of the healthy lines remains nearly sinusoidal. If the absolute value is considered, the skewness coefficient is left-skewed, with a value close to -0.5, and the waveforms for both half-cycle and full-cycle are almost identical. Thus, the skewness coefficients for the half-cycle and full-cycle remain similar. However, for the faulty line, the zero-sequence current waveform becomes distorted near the zero-crossing point. Once the absolute value is taken, the probability distribution of the sampled values becomes asymmetrical and skewed to the right. By computing skewness over several cycles and combining full-cycle and half-cycle values, the proposed scheme suppresses the influence of occasional measurement noise while enhancing the directional asymmetry introduced by HIF. The expression for calculating skewness is as follows:

$$S_{i0(\frac{T\alpha}{2}),q}=\frac{\sum_{N=\frac{T\alpha}{2}}^{N=\frac{T}{2}(1+\alpha)}\left(\frac{|i(N)|-\mu_{\frac{T\alpha}{2},q}}{\sigma_{\frac{T\alpha}{2},q}}\right)^3}{N/2-1} \tag{7}$$

Decision-making process of fault diagnosis

Based on the analysis above, the novel decision-making process for diagnosing HIF is illustrated in Fig. 1. To enhance sensitivity to early-stage or incipient HIF, the decision-making framework incorporates an initial physical triggering mechanism before applying the statistical analysis. Even when the fault arc is weak and the kurtosis or skewness characteristics are not yet fully developed, the zero-sequence voltage typically experiences a measurable rise due to grounding asymmetry. This early indication is used as a preliminary fault-suspicion signal, ensuring that the subsequent kurtosis–skewness evaluation is performed only once the waveform distortion becomes sufficiently observable for reliable statistical discrimination.

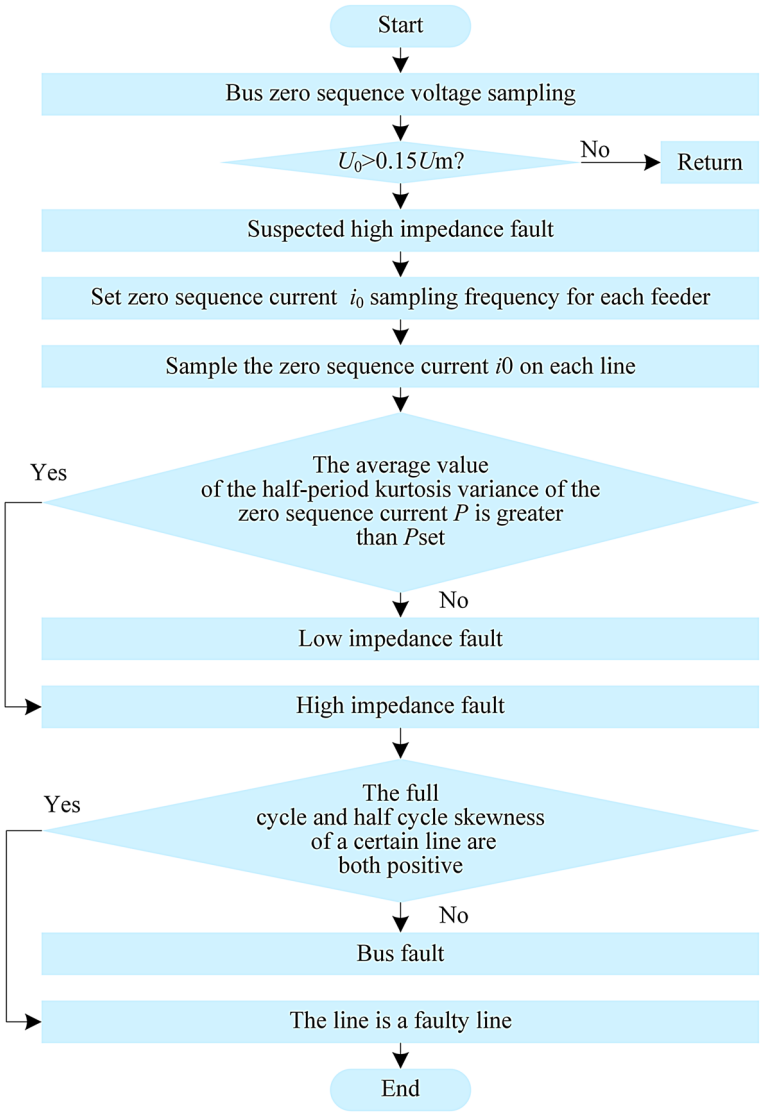

Fig. 1. Novel Fault Diagnosis Decision-Making Process Flowchart.

Step 1 Begin by sampling and recording the zero-sequence voltage U_0 of the bus. If the effective value exceeds 0.15 times the phase voltage and the zero-sequence voltage protection of the system has not yet been triggered, a HIF is suspected in the system [26].

Step 2 Set the sampling frequency of the zero-sequence current i_{0q} for each feeder to 10 kHz. Record the zero-sequence current i_{0q} for each line over 20 power frequency cycles, and using half-cycle sampling data, calculate the kurtosis of the zero-sequence current for each line as per (3).

Step 3 Apply (4) to calculate the kurtosis variance for each line, then use (5) to determine the overall average value P. If P exceeds the preset threshold Pset, proceed to *Step 4* and classify the fault as a HIF; otherwise, it is considered a common fault, and the process returns to *Step 1*.

Step 4 Take 200 samples of zero-sequence current data within one cycle and compute the full-cycle skewness value $S_{0q}(j)$ for each line using (7). Then, with 100 samples of half-cycle data, calculate the half-cycle skewness value $M_{0q}(j)$.

Step 5 Once the skewness values stabilize, calculate the full-cycle skewness average p_{0q} and the half-cycle skewness average q_{0q} for each line as follows:

$$p_{0q} = \frac{\sum_{j=1}^{10} S_{0q}(j)}{10} \tag{8}$$

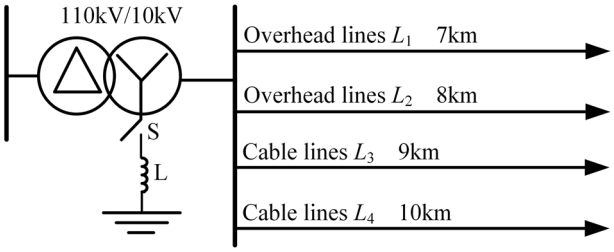

Fig. 2. Model of the Resonant Grounding System.

Type of line	Impedance (Ω/km)		Inductance (mH/km)		Capacitance to ground (μF/km)	
	Positive sequence	Zero sequence	Positive sequence	Zero sequence	Positive sequence	Zero sequence
Overhead lines	0.178	0.25	1.21	0.54	0.01	0.006
Cable lines	0.27	2.7	0.255	1.02	0.339	0.28

Table 1. Line parameters of the simulation model.

Type of line	Short-circuit position/km	Kurtosis *variance*		
		100Ω	500Ω	1000Ω
Overhead lines	1	1.93e-8	1.97e-9	6.02e-7
	3	**1.81e-7**	**1.04e-7**	**1.03e-6**
	5	1.35e-7	4.71e-8	9.76e-7
	7	5.33e-8	2.27e-8	6.14e-7
Cable lines	1	3.59e-9	3.12e-10	3.57e-7
	3	2.74e-10	3.25e-11	5.29e-7

Table 2. Mean kurtosis variance for LIFs.

$$q_{0q} = \frac{\sum_{j=11}^{30} M_{0q}(j)}{20} \tag{9}$$

Step 6 If a line q exhibits both p_{0q} and q_{0q} greater than 0, the line q is identified as the HIF line. If not, the fault is located at the bus.

Simulation analysis of single-phase grounding fault

Simulation model

The HIF diagnosis for the resonant grounding system is verified using MATLAB/Simulink for the distribution network depicted in Fig. 2. The 10 kV medium voltage distribution system consists of two overhead lines (L_1, L_2) and two cable lines (L_3, L_4), with the corresponding line parameters provided in Table 1. The switch S is closed, and the arc suppression coil is over-compensated by 10%. The active power of the load is set at 1 MW, with a power factor of 0.89, and the load model is three-phase symmetrical. The system sampling frequency is configured to 10 kHz [27]. Following a fault occurrence, the zero-sequence current for each feeder is recorded through sampling. In the simulations, fault locations are set on different outgoing lines with line lengths and parameters given in Table 1, and the transition resistance is varied from 5 kΩ to 20 kΩ with multiple initial fault phase angles so that a broad range of realistic HIF scenarios can be examined, consistent with the parameter ranges reported in [27].

Threshold setting of kurtosis coefficient

In general, a fault is classified as low impedance if the transition impedance of a single-phase short circuit is below 1 kΩ. Considering the zero-sequence voltage protection configured for medium-voltage distribution networks, the critical fault impedance threshold for traditional protection systems is approximately 100Ω [28]. In this study, we define the range between 100Ω and 1 kΩ as low impedance. The mean kurtosis variance values for different line types and various short-circuit locations are calculated accordingly, with the results presented in Table 2.

In Table 2, it is evident that the mean kurtosis variance of the cable line is significantly smaller than that of the overhead line. Specifically, for the overhead line, the kurtosis variance mean value is notably higher for short circuits occurring at the 3 km mark. Figs. 3(a)-(d) illustrates the typical mean kurtosis variance for LIFs under varying impedance values and initial phases. The largest mean kurtosis variances for LIFs are observed

around 1 kΩ. As the impedance increases, the mean kurtosis variance declines with some fluctuations. It was determined that when the kurtosis variance of the zero-sequence current exceeds 1e-4, the fault is classified as high impedance. If the value is lower, it is considered a LIF. To account for a margin of safety, the threshold *P*set is set to 0.002.

Simulation verification of decision-making method

Using the simulation model of the resonant grounding system shown in Fig. 2, the following parameters are applied: R_p= 1500Ω, R_n= 1000Ω, V_p= 2000 V, and V_n= 1500 V. At 0.04 s, a single-phase high-impedance ground fault occurs on feeder L_2, located 2 km from the bus, with a fault clearing angle of 0°.

The half-cycle kurtosis coefficients of the zero-sequence current, calculated for all lines, are shown in Fig. 4(a), while Fig. 4(b) presents the same for a fault on L_1. Each subfigure includes curves K_1 to K_4 corresponding to all four feeders.

Approximately one cycle after the fault, the kurtosis value for the faulted feeder spikes and then stabilizes around a certain level. The average variance of these kurtosis values across all lines is computed and found to be P = 0.0028 for L_2 and 0.0025 for L_1, respectively, both exceeding the defined threshold. These results confirm the presence of HIF. To identify the specific faulted line, full-cycle skewness and half-cycle skewness of the zero-sequence current are analyzed.

Fig. 4(c) and Fig. 4(d) present the full-cycle skewness coefficients S_{01} to S_{04}, while Fig. 4(e) and Fig. 4(f) show the half-cycle skewness coefficients M_{01} to M_{04} for faults on L_2 and L_1, respectively. It is observed that after three cycles, the full-cycle skewness for the faulted feeder (L_2 in one case, L_1 in another) stabilizes above zero (e.g., around 0.35 for L_2 and 0.3077 for L_1), whereas other lines remain below zero. Similarly, the half-cycle skewness for the faulted lines fluctuates near 0.3 (e.g., 0.1927 for L_1), and again, other lines remain below zero. These contrast patterns enable accurate faulted-line identification.

Without changing the line parameters or location, a LIF is introduced at 0.04 s on feeder L_2 with a grounding resistance of 100 Ω. The kurtosis coefficients for this scenario are shown in Fig. 5. The threshold was further verified through extensive parameter sweeping under different impedances, sampling frequencies, and background noise levels to confirm its adaptability to varying network conditions. The sampling rate of 10 kHz and the use of a 20-cycle observation window follow the recommendations in [27], which demonstrate that such settings provide sufficient resolution for identifying arc-induced nonlinearity while ensuring acceptable detection latency. After three cycles, kurtosis values across all lines stabilize, but the calculated variance is only 1.9×10^{-8}, significantly below the 0.002 threshold.

This result clearly demonstrates that the proposed kurtosis-based variance threshold effectively distinguishes between high-impedance and low-impedance ground faults.

Reliability verification

To further validate the reliability of the proposed method, Table 3 presents simulation results for multiple single-phase grounding faults occurring on different outgoing lines, with varying conditions of random fault locations, transition impedance, and initial fault phase angles. The table clearly shows that the mean kurtosis variance effectively captures the characteristics of HIF. Moreover, accurate fault line selection is achieved by combining the mean full-cycle and half-cycle skewness values. This trend is consistent with recent work on incipient fault detection in inverter systems, where intensive multiorder feature extraction is used to highlight subtle deviations from healthy operation before they evolve into severe faults[29]. The cases in Table 3 are obtained by combining several fault positions on lines $L1_1$–L_4, transition resistances within 5–20 kΩ and different initial fault phase angles. A summary row has been added at the bottom of Table 3 to report the total numbers of correct and false detections across all scenarios.

The cases in Table 3 are generated by combining multiple fault locations, transition resistances and initial phase angles. The table now includes the total number of correct and false detections to summarize the overall performance.

Test of the robustness under noise

As the SNR ratio decreases, noise imposes greater interference on the waveform. Fig. 6 illustrates the kurtosis curve obtained by introducing white noise at SNR ratios of 30 dB and 20 dB, respectively, into the zero-sequence

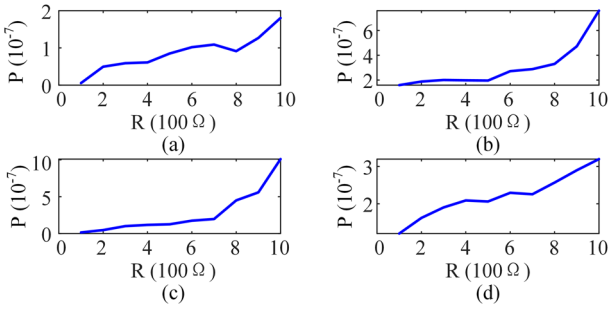

Fig. 3. Dependence of LIF Kurtosis on Initial Phase: (a) initial phase: 0°, (b) initial phase: 30°,. (c) initial phase: 60°, (d) initial phase: 90°.

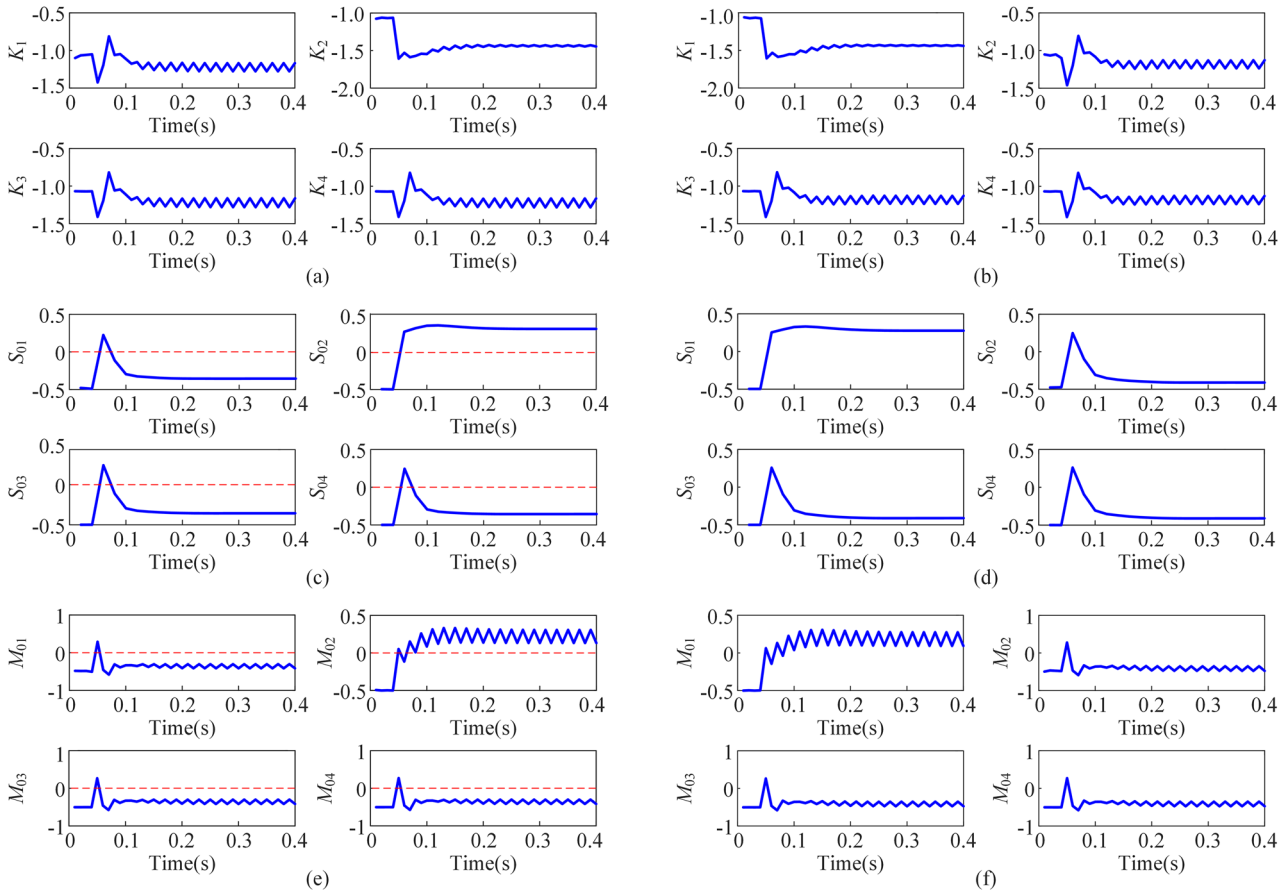

Fig. 4. Characteristic Coefficients of Zero-Sequence Current under HIF Conditions in L_1 and L_2: (a) kurtosis coefficients of the zero-sequence current in L_2, (b) kurtosis coefficients of zero-sequence current in L_1, (c) full-cycle skewness coefficients in L_2, (d) full-cycle skewness coefficients in L_1, (e) half-cycle skewness coefficients in L_2, (f) half-cycle skewness coefficients in L_1.

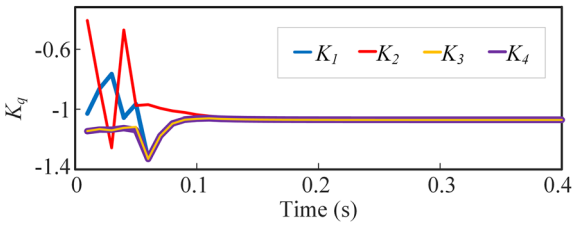

Fig. 5. Kurtosis Coefficients of Zero-Sequence Current (LIF in L_2).

current signal during high- and low-impedance grounding faults on line L_2. It is evident that the fluctuation range of the half-cycle kurtosis value for LIFs is significantly narrower compared to HIF. When the white noise level is 30 dB, the mean kurtosis variance for the HIF is 0.0026, while for the LIF, it is 5.7e-6. At a white noise level of 20 dB, the mean kurtosis variances are 0.0046 and 4.46e-5, respectively. Despite the noise, the set threshold can still reliably identify HIF.

To comprehensively evaluate the robustness of the proposed detection method under realistic noise interference, six representative HIF detection approaches were selected for comparison under the same single-phase high-impedance ground fault conditions analyzed earlier. These approaches span time-domain, frequency-domain, time–frequency domain, and AI-based techniques. Table 4 examines whether the characteristic quantities extracted by each method continue to satisfy their respective threshold criteria when subjected to multiple SNR levels, thereby revealing the sensitivity of each algorithm to noise-induced distortion.

In Table 4, the detection methods are indexed from 1 to 6 according to their order of appearance. The suffix 'exceed' indicates that a value above the threshold is interpreted as a fault, while 'below' denotes that a value falling below the threshold triggers a fault decision. The comparative results demonstrate that the time-domain

φ/°	Transition impedance		Kurtosis *variance*	Fault type	Mean Full-cycle skewness p_{0q}				Mean half-cycle skewness q_{0q}				Fault line	Correct or false
	R_p	R_n			p_{01}	p_{02}	p_{03}	p_{04}	q_{01}	q_{02}	q_{03}	q_{04}		
90	550	500	**0.0037**	HIF	**0.5060**	-0.3346	-0.3342	-0.3337	**0.4450**	-0.3222	-0.3219	-0.3215	L_1	Correct
90	1500	1000	**0.0281**	HIF	**0.6562**	-0.3970	-0.3972	-0.3965	**0.5035**	-0.3798	-0.3801	-0.3795	L_1	Correct
90	2000	1500	**0.0026**	HIF	**0.3505**	-0.3939	-0.3943	-0.3939	**0.2254**	-0.3811	-0.3816	-0.3812	L_1	Correct
60	550	500	**0.0044**	HIF	-0.3502	**0.6716**	-0.3487	-0.3489	-0.3341	**0.4467**	-0.3326	-0.3328	L_2	Correct
60	1500	1000	**0.0285**	HIF	-0.3970	**0.6564**	-0.3973	-0.3966	-0.3798	**0.5019**	-0.3802	-0.3796	L_2	Correct
60	2000	1500	**0.0060**	HIF	-0.4100	**0.4509**	-0.4110	-0.4104	-0.3938	**0.3400**	-0.3946	-0.3941	L_2	Correct
30	550	500	**0.005**	HIF	-0.3529	-0.3529	-0.3508	-0.3506	-0.3389	-0.3389	-0.3371	-0.3365	bus	Correct
30	1500	1000	**0.0028**	HIF	-0.3983	-0.3984	-0.3980	-0.3976	-0.3821	-0.3821	-0.3820	-0.3811	bus	Correct
30	2000	1500	**0.0021**	HIF	-0.4124	-0.4125	-0.4129	-0.4105	-0.3956	-0.3956	-0.3961	-0.3952	bus	Correct
0	500		**3e-8**	LIF	-0.5496	-0.5490	-0.5491	-0.5491	-0.5273	-0.5267	-0.5268	-0.5267		
30	1000		**6e-7**	LIF	-0.5501	-0.5494	-0.5492	-0.5490	-0.5278	-0.5270	-0.5269	-0.5268		

Table 3. HIF diagnosis results under various factors.

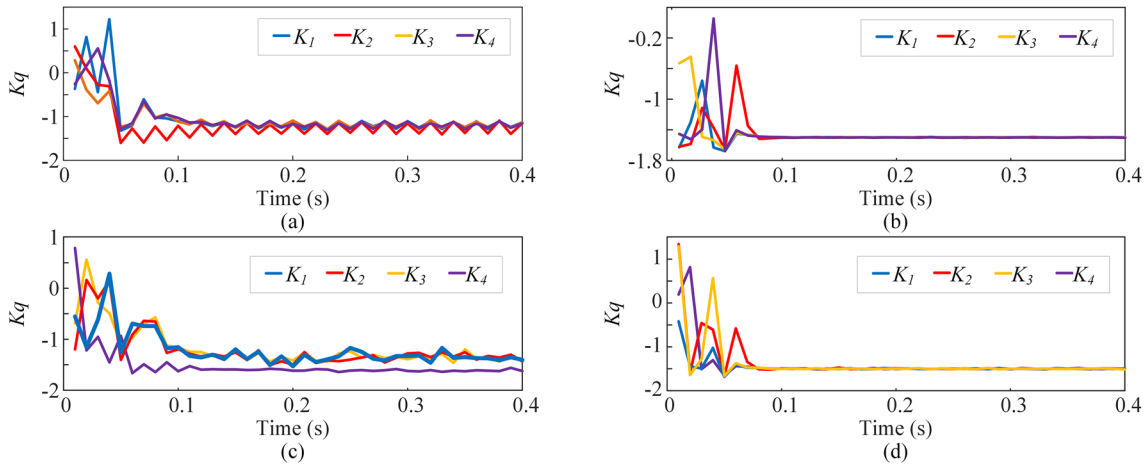

Fig. 6. Test Results Under Different Noise Levels: (a) kurtosis coefficient of HIF with 30db of white noise, (b) kurtosis coefficient of LIF with 30db of white noise, (c) kurtosis coefficient of HIF with 20db of white noise,. (d) kurtosis coefficient of LIF with 20db of white noise.

Method	Detection method	Values of feature quantities				Set threshold	Recognition time (s)	Correct or false
		30db	20db	15db	10db			
1	Based on fault phase voltage polarization (time domain)[30]	0.224	0.173	0.256	0.249	0.3 (exceed)	23.16	False
2	Interharmonic-based (frequency domain)[28]	0.378	0.405	0.573	0.699	0.4 (exceed)	129.57	False
3	Based on zero-sequence voltage spectrum (frequency domain)[31]	0.0257	0.0216	0.0204	0.0187	0.02 (below)	167.55	False
4	Hybrid wavelet algorithm (time-frequency domain)[32]	0.198	0.210	0.262	0.293	0.15 (exceed)	205.38	Correct
5	Based on wavelet energy moments (time-frequency domain)[23]	2.147	4.268	5.36	5.57	0 (exceed)	303.92	Correct
6	D-S fusion judgment (artificial intelligence)[33]	0.59	0.677	0.725	0.839	0.5 (exceed)	497.13	Correct
	Proposed method	**0.0026**	**0.0046**	**0.0052**	**0.0055**	**0.002 (exceed)**	**100.18**	**Correct**

Table 4. Detection methods affected by different SNRs.

voltage polarization method (Method 1) is highly sensitive to noise, with its extracted feature values fluctuating near the threshold across all SNR conditions, resulting in unstable or incorrect HIF identification. Among the frequency-domain methods, the interharmonic-based approach (Method 2) exhibits stronger noise tolerance, consistently maintaining a detectable margin at 20 dB, whereas the zero-sequence spectrum method (Method 3) shows significant degradation as the SNR decreases, indicating limited robustness to high noise.

The proposed kurtosis–skewness method maintains a significantly more stable margin between the characteristic feature and the threshold, even at 30 dB, and achieves substantially shorter recognition time. The hybrid wavelet algorithm and wavelet energy moment method (Methods 4 and 5), which fuse time-domain and

frequency-domain information, demonstrate higher resilience against noise; however, they incur considerable computational cost, with the longest processing time reaching 303.92 s, which is 203.37% higher than that of the proposed approach (100.18 s). Similarly, the AI-based D-S fusion method (Method 6) maintains good convergence margins but suffers from an even higher computation time of 497.13 s, corresponding to a 392.24% increase relative to the proposed algorithm.

For broader methodological context, recent learning-based reliability frameworks such as[34,35] employ deep neural architectures to extract features, assess degradation and forecast reliability in capacitor-bank applications. These approaches integrate analog and digital measurements and require training datasets to build their reliability models. The present study pursues a different objective, focusing on real-time high-impedance fault detection in resonant grounding systems using directly computed kurtosis and skewness indices. Because the proposed method operates without a training phase or reliability-forecasting modules, its structural complexity and data dependency remain low, while still providing stable detection performance under noise and load-imbalance conditions.

Overall, the proposed detection framework achieves a favorable balance between computational efficiency and robustness against noise interference. It delivers fast response, reliable threshold separation, and accurate fault identification even in challenging low-SNR environments, demonstrating its practicality for real-world resonant grounding applications.

The impact of three-phase load imbalance on the detection results

In this section, a simulation of three-phase load imbalance in the transmission line is conducted. By adjusting the active power of the three-phase load, the imbalance degree is varied between 10% and 50%, while keeping the source voltage, transformer, and line parameters unchanged. The simulation results of the proposed algorithm are summarized in Table 5. For this simulation, the grounding resistance was set at 1 kΩ, and the fault was positioned 7 km along Line L_2.

As indicated in Table 5, under conditions of three-phase load imbalance, the kurtosis value consistently increases with the growing imbalance, and the magnitude of this change far exceeds the detection threshold. This suggests that kurtosis is a key feature for the identification of HIF. The underlying cause can be attributed to load imbalance, which introduces asymmetry in the three-phase line voltages, thereby causing the zero-sequence voltage to exhibit a significantly larger amplitude sinusoidal characteristic, ultimately resulting in elevated kurtosis values. Although the skewness value does not show a clear trend, the skewness for Line L_2 is notably positive, thereby identifying L_2 as the faulted line. In summary, the proposed method proves effective in detecting HIF under conditions of three-phase load imbalance. These results indicate that the statistical thresholds remain valid over a wide range of load imbalance degrees, and that the kurtosis–skewness features continue to distinguish the faulted feeder without requiring re-tuning for each operating condition.

Scalability verification

Real distribution network laboratory testing

To further validate the effectiveness of the proposed method, experiments were conducted in a laboratory setup using a 10 kV distribution network. In the experimental configuration, the 10 kV busbar is connected to four feeders, with the neutral point grounded via an arc suppression coil. The wiring diagram of the experimental system is shown in Fig. 7, with specific parameters outlined in Table 6. In this setup, CT denotes the current transformer used for zero-sequence current acquisition, and PT refers to the potential transformer used for measuring the zero-sequence voltage of the bus. It is worth noting that the topology, line parameters and grounding configuration of this experimental network differ from those used in the simulation model, yet the same kurtosis–skewness indices and threshold settings are applied without re-tuning, which demonstrates that the proposed method can be transferred across different systems with only limited offline adjustment. After a single-phase ground fault occurs in the detection system, the control system of the setup sends commands to the controllable voltage source. This allows for regulation of the input voltage on the secondary side of the injection transformer, which, after being stepped up, is connected to the neutral point of the distribution network, enabling control over both the amplitude and phase of the zero-sequence voltage.

Imbalance degree	Kurtosis *variance*	Mean Full-cycle skewness p_{0q}				Mean half-cycle skewness q_{0q}				Correct or false
		p_{01}	p_{02}	p_{03}	p_{04}	q_{01}	q_{02}	q_{03}	q_{04}	
Normal	0.0033	-0.3886	**0.6562**	-0.3663	-0.3517	-0.2996	**0.4915**	-0.3539	-0.3668	Correct
10%	0.0037	-0.3457	**0.6213**	-0.3544	-0.3359	-0.3002	**0.5226**	-0.3497	-0.3572	Correct
15%	0.00281	-0.3596	**0.6668**	-0.3541	-0.3442	-0.3163	**0.4523**	-0.2651	-0.3668	Correct
20%	0.0026	-0.2966	**0.6039**	-0.3554	-0.3226	-0.3026	**0.4539**	-0.2518	-0.3233	Correct
25%	0.0029	-0.3056	**0.5699**	-0.3441	-0.3236	-0.3066	**0.4882**	-0.3217	-0.3537	Correct
30%	0.0031	-0.3122	**0.6017**	-0.3541	-0.3228	-0.2773	**0.4786**	-0.3326	-0.3531	Correct
35%	0.0035	-0.3284	**0.5774**	-0.3596	-0.3429	-0.3234	**0.4883**	-0.3417	-0.3546	Correct
40%	0.0035	-0.3546	**0.6067**	-0.3541	-0.3623	-0.3001	**0.4826**	-0.3425	-0.3531	Correct
45%	0.0037	-0.3283	**0.6132**	-0.3503	-0.3627	-0.3026	**0.4739**	-0.3235	-0.3113	Correct
50%	0.0039	-0.3756	**0.5992**	-0.3183	-0.3427	-0.3376	**0.4835**	-0.3037	-0.2988	Correct

Table 5. The impact of three-phase load imbalance on the detection results.

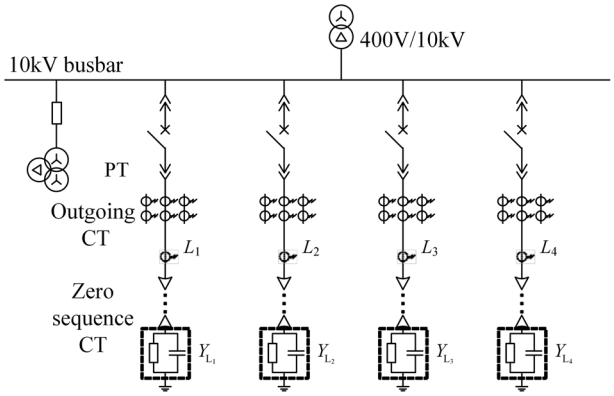

Fig. 7. Topological Structure of the 10 kV Distribution Network System.

Parameter	Value
System rated voltage (kV)	10.5
Injection transformer capacity (kVA)	2500
Grounding transformer capacity (kVA)	100
System grounding capacitive current (A)	97.5
Damping ratio (%)	2.6

Table 6. Experimental parameters of typical 10kVdistribution network.

Impedance (kΩ)	Kurtosis variance	Fault type	Mean full-cycle skewness p_{0q}				Mean half-cycle skewness q_{0q}				Fault line selection	Correct or false
			p_{01}	p_{02}	p_{03}	p_{04}	q_{01}	q_{02}	q_{03}	q_{04}		
5	0.0355	HIF	-0.3396	-0.4569	-0.4779	**0.5639**	-0.3689	-0.3775	-0.4936	**0.3789**	L_4	Correct
10	0.0309	HIF	-0.3674	-0.4237	-0.4055	**0.6126**	-0.3551	-0.3160	-0.3899	**0.3953**	L_4	Correct
20	0.0287	HIF	-0.3662	-0.4537	-0.3767	**0.5716**	-0.3549	-0.3941	-0.3854	**0.3569**	L_4	Correct

Table 7. Zero-sequence current kurtosis and skewness calculation results for three branch Lines.

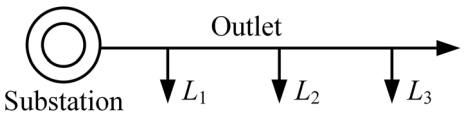

Fig. 8. Primary Wiring Diagram of a Substation Line Side.

Single-phase ground faults of 5 kΩ, 10 kΩ, and 20 kΩ occurred on line L_4 at 0.1 s. After filtering the zero-sequence current data for each line, the corresponding kurtosis and skewness values are summarized in Table 7. Once ground fault, the kurtosis of the line steadily decreases as the fault transition resistance rises from 5 kΩ to 20 kΩ. Despite this reduction, the kurtosis remains above the predefined threshold. Moreover, regardless of varying operating conditions, the proposed method reliably identifies the faulted line using skewness.

Field test

Field recording data confirm the effectiveness of the proposed method. A 10 kV substation is selected as a representative example of a resonant grounding system, with the wiring diagram shown in Fig. 8.

The zero-sequence current distribution of L_2 during a single-phase high-impedance grounding fault is recorded and depicted in Fig. 9. The zero-sequence currents for L_1, L_2, and L_3 are denoted as i_{01}, i_{02}, and i_{03}, respectively.

In this instance, the kurtosis variance calculated using the proposed method, along with the zero-sequence current skewness values for each line, is presented in Table 8.

Following the fault diagnosis procedure in Fig. 1, the mean value of the zero-sequence current kurtosis variance is calculated as 0.0318, significantly exceeding the threshold of 0.002. The zero-sequence current deviation for each branch is also determined, with only the second branch showing a positive value for both

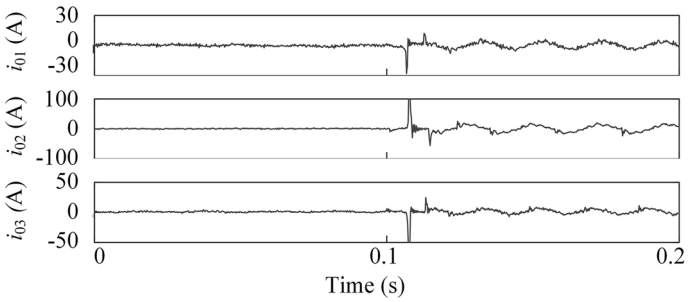

Fig. 9. Zero-Sequence Current Waveform for Three Outgoing Lines.

Kurtosis variance	Fault type	Mean full-cycle skewness p_{0q}			Mean half-cycle skewness q_{0q}			Fault line selection	Correct or false
		p_{01}	p_{02}	p_{03}	q_{01}	q_{02}	q_{03}		
0.0318	HIF	-0.3267	**0.5038**	-0.5335	-0.3145	**0.3576**	-0.5174	L_2	Correct

Table 8. Zero-sequence current kurtosis and skewness calculation results for three branch lines.

Kurtosis variance	Fault type	Mean full-cycsle skewness p_{0q}			Mean half-cycle skewness q_{0q}			Fault line selection	Correct or false
		p_{01}	p_{02}	p_{03}	q_{01}	q_{02}	q_{03}		
0.0036	HIF	**0.4562**	-0.2781	-0.3042	**0.3271**	-0.2761	-0.4123	L_1	Correct
0.0041	HIF	-0.4853	-0.2314	**0.5721**	-0.2734	-0.2385	**0.4382**	L_3	Correct
2e-5	LIF	-0.2076	-0.3092	-0.4378	-0.5394	-0.5783	-0.5842	/	Correct

Table 9. Zero-sequence current kurtosis and skewness calculation results.

full-cycle and half-cycle deviations, while the rest are negative. This clearly identifies a HIF on the L_2 branch. Verified by actual substation data, the proposed method is effective for identifying HIF in branch lines of outgoing feeders. The preset kurtosis threshold can easily distinguish HIF, further demonstrating the accuracy and reliability of the method.

To further validate this approach, additional recorded wave data from other substations with grounding faults were analyzed. The results, shown in Table 9, confirm that both high- and low-resistance faults can still be identified accurately. These field results are in line with the broader evolution of reliability-oriented monitoring, where statistically derived health indicators are embedded into remaining useful life prediction and long-term reliability assessment frameworks for safety-critical components.

Conclusion

This paper introduces a novel statistical approach for high-impedance fault detection in resonant-grounded distribution networks by jointly analyzing the kurtosis and skewness characteristics of zero-sequence current waveforms. Building on the Emanuel arc model, the method identifies HIFs through a kurtosis-variance index and then locates the faulted feeder using full-cycle and half-cycle skewness indicators. Simulation studies show that the kurtosis variance of HIFs increases significantly compared to normal conditions, achieving values around 0.0318 while remaining clearly above the detection threshold. The method demonstrates strong robustness under low SNR conditions, maintaining stable detection margins even at 20 dB and 30 dB noise levels. Compared with existing time-domain, frequency-domain, and wavelet-based techniques, the proposed scheme achieves reliable detection with substantially lower computation time, making it suitable for practical engineering applications.

Laboratory testing on a 10 kV resonant-grounded network and field measurements further confirm the method's adaptability under real operating conditions, including different feeder types and grounding configurations. Although early-stage faults with weak distortion and rapidly changing operating states in active distribution networks may still challenge detection, these limitations can be addressed through adaptive thresholds and enhanced feature extraction. The proposed framework therefore offers a simple, noise-resilient, and computationally efficient alternative to traditional HIF detection techniques, providing a strong basis for future extensions incorporating distributed generation, data-driven adaptability, and large-scale system validation.

Data availability

Data will be made available by contacting qinglin.meng@ieee.org.

Received: 6 September 2024; Accepted: 16 December 2025
Published online: 05 January 2026

References

1. Chen, J. et al. Current spectral norm and phase variation based fault region identification for active distribution network. *Sci. Rep.* **14** (1), 12640 (2024).
2. Liu, H. et al. Novel fault current elimination method for modular multilevel DC/DC converter based on hybrid HBSM and TDM. *CSEE J. Power Energy Syst.* **Early Acce**, 1–11 (2024). Online. https://doi.org/10.17775/CSEEJPES.2023.07350
3. Xu, X. et al. Reconfiguration of low-voltage distributed power sources within electric power's distribution network based on improved particle swarm-fish swarm fusibility algorithm. *Sci. Rep.* **14** (1), 5444 (2024).
4. Meng, Q., Jin, X., Luo, F., Wang, Z. & Hussain, S. Distributionally robust scheduling for benefit allocation in regional integrated energy system with multiple stakeholders. *J. Mod. Power Syst. Clean. Energy*. **12** (5), 1631–1642 (2024).
5. Wei, J., Liang, F., Feng, H. & Ran, L. Condition monitoring of discrete power devices: A data-driven approach with stress quantification and mold temperature sensing. *IEEE J. Emerg. Sel. Top. Power Electron.* **12** (3), 2569–2579 (2024).
6. Li, Y., Zhang, S., and Li, Y. AI-enhanced resilience in power systems: adversarial deep learning for robust short-term voltage stability assessment under cyber-attacks. Chaos, Solitons & Fractals, **196**, 116406 (2025).
7. Yousaf, M. Z. et al. Bayesian-optimized LSTM-DWT approach for reliable fault detection in MMC-based HVDC systems. *Sci. Rep.* **14** (1), 17968 (2024).
8. Wei, X., Wang, X., Gao, J., Wang, B. & Yang, D. High impedance fault detection based on Arc changing tendency and nonlinear least squares for active distribution networks. *IEEE Trans. Ind. Inf.* **20** (6), 8572–8584 (2024).
9. Li, B. et al. Study on the calculation method of electrical quantity for connection line open-phase operation of wind farm connected to MMC-HVDC considering negative sequence current suppression. *Int. J. Electr. Power Energy Syst.* **159**, 110056 (2024).
10. Salama, M. et al. Boosting piezoelectric properties of PVDF nanofibers via embedded graphene oxide nanosheets. *Sci. Rep.* **14** (1), 16484 (2024).
11. Wang, W., Gao, X., Fan, B., Zeng, X. & Yao, G. Faulty phase detection method under single-line-to-ground fault considering distributed parameters asymmetry and line impedance in distribution networks. *IEEE Trans. Power Deliv.* **37** (3), 1513–1522 (2021).
12. Sun, D., Liu, H., Liu, S. & Bi, T. Development of synchronized waveform measurement and its application on fault detection. *IEEE Trans. Instrum. Meas.* **72**, 1–11 (2023).
13. Ge, Q., Ren, L. & Li, J. Study on the algorithm of fault recording analysis combining its time-domain waveforms with phase-domain trajectories. *Sci. Rep.* **14** (1), 4435 (2024).
14. Srivastava, A. K., Tiwari, A. N. & Singh, S. N. Harmonic and interharmonic Estimation using poincaré filtering assisted ESPRIT method. *IEEE Trans. Ind. Appl.* **59** (4), 4859–4867 (2023).
15. Arpanahi, M. K., Fini, M. H., Sanaye-Pasand, M. & Ghorbani, A. Generalized equivalent circuit and algorithm for single-end fault location in transmission systems. *IEEE Trans. Ind. Inf.* **20** (3), 4863–4873 (2023).
16. Li, M. et al. Scaling-basis chirplet transform. *IEEE Trans. Ind. Electron.* **68** (9), 8777–8788 (2020).
17. Li, B., Zheng, D., Li, B. et al. Research on low voltage ride-through strategies for doubly-fed wind farms during asymmetric faults. *International Journal of Electrical Power & Energy Systems*, **160**, 110138 (2024). DOI: 10.1016/j.ijepes.2024.110138.
18. Jiang, T. et al. Forced Oscillation source location of bulk power systems using synchrosqueezing wavelet transform. *IEEE Trans. Power Syst.* **39** (5), 6689–6701 (2024).
19. Yuan, J. & Jiao, Z. Faulty-feeder detection for single phase-to-ground faults in distribution networks based on waveform encoding and waveform segmentation. *IEEE Trans. Smart Grid.* **14** (5), 4100–4115 (2023).
20. Gadanayak, D. A., Mishra, M. & Bansal, R. C. High impedance fault detection in distribution networks using randomness of zero-sequence current signal: A detrended fluctuation analysis approach. *Appl. Energy*. **368**, 123452 (2024).
21. Bai, H., Gao, J. H., Li, W., Wang, K. & Guo, M. F. Detection of high-impedance fault in distribution networks using frequency-band energy curve. *IEEE Sens. J.* **24** (1), 427–436 (2023).
22. Zhao, N., Zhao, T., Cao, J. & Shi, H. Fault diagnosis of dual-network recursive interval type-2 fuzzy neural network based on SVD-TLS optimization. *Comput. Ind. Eng.* **207**, 111280 (2025).
23. Wang, H., Li, Y. F., Men, T. & Li, L. Physically interpretable wavelet-guided networks with dynamic frequency decomposition for machine intelligence fault prediction. *IEEE Trans. Syst. Man. Cybern Syst.* **54** (8), 4863–4875 (2024).
24. Zhang, C., Wang, H., Wang, Z. & Li, Y. Active detection fault diagnosis and fault location technology for LVDC distribution networks. *Int. J. Electr. Power Energy Syst.* **148**, 108921 (2023).
25. Li, Y., Cao, J., Xu, Y. et al."Deep learning based on Transformer architecture for power system short-term voltage stability assessment with class imbalance," Renewable and Sustainable Energy Reviews, **189**, 113913 (2024). DOI: 10.1016/j.rser.2023.113913.
26. Li, L., Gao, H., Yuan, T., Peng, F. & Xue, Y. Location method of high-impedance fault based on transient zero-sequence factor in non-effectively grounded distribution network. *Electr. Power Syst. Res.* **226**, 109912 (2024).
27. Biswal, M., Ghore, S., Malik, O. P. & Bansal, R. C. Development of time-frequency based approach to detect high impedance fault in an inverter interfaced distribution system. *IEEE Trans. Power Deliv.* **36** (6), 3825–3833 (2021).
28. Mohammadi, M., Karimi, G. & Sarabi, H. G. Design of a microstrip Wilkinson power divider using a low pass filter with the particle swarm optimization algorithm. *Sci. Rep.* **14** (1), 17637 (2024).
29. Wang, M., Cheng, F., Xie, M., Qiu, G. & Zhang, J. Intensive multi-order feature extraction for incipient fault detection of inverter system. *IEEE Trans. Power Electron.* **40** (2), 3543–3552 (2024).
30. Zhang, H. et al. A novel practical criteria in detecting high impedance earth faults based on single-phase PT isolated distribution system, in., *IEEE Industry Applications Society Annual Meeting (IAS)*, (2023) 1–8. (2023).
31. Liu, H., Yang, Q., Tang, L., Yuan, T. & Zhou, T. Fault type identification of Arc grounding based on time-frequency domain characteristics of zero sequence current. *Electr. Power Syst. Res.* **223**, 109689 (2023).
32. Naderi, E., Mirzaei, L., Trimble, J. P. & Cantrell, D. A. Multi-objective optimal power flow incorporating flexible alternating current transmission systems: application of a wavelet-oriented evolutionary algorithm. *Electr. Power Compon. Syst.* **52** (5), 766–795 (2024).
33. Wei, X. et al. Faulty feeder detection based on fundamental component shift and multiple-transient-feature fusion in distribution networks. *IEEE Trans. Smart Grid*. **12** (2), 1699–1711 (2020).
34. Rezaei, M. A. et al. Adaptation of a real-time deep learning approach with an analog fault detection technique for reliability forecasting of capacitor banks used in mobile vehicles. *IEEE Access.* **10**, 132271–132287 (2022).
35. Rezaei, M. A. et al. Reliability calculation improvement of electrolytic capacitor banks used in energy storage applications based on internal capacitor faults and degradation. *IEEE Access.* **12**, 13146–13164 (2024).

Author contributions

Qinglin Meng: Conceptualization, Visualization, Project Administration, Writing - Original Draft. Yuan Gao: Methodology, Software, Data Curation. Sheharyar Hussain: Formal Analysis, Writing - Review & Editing. Ying He: Investigation, Funding Acquisition. Botong Li: Resources, Supervision, Validation.

Declarations

Competing interests

The authors declare no competing interests.

Additional information

Correspondence and requests for materials should be addressed to Q.M., Y.G., S.H., Y.H. or B.L.

Reprints and permissions information is available at www.nature.com/reprints.

Publisher's note Springer Nature remains neutral with regard to jurisdictional claims in published maps and institutional affiliations.